metals

MDPI

Article

Evolution of Metal Surface Topography during Fatigue

Darong Zhu [1,2], Lu Xu [1,2], Fangbin Wang [1,2,*], Tao Liu [1,2] and Ke Lu [2,3]

1 School of Mechanical and Electrical Engineering, Anhui Jianzhu University, Hefei 230601, China; gkj@ahjzu.edu.cn (D.Z.); xulu19910627@gmail.com (L.X.); Liutao19841015@163.com (T.L.)
2 Key Laboratory of Construction Machinery Fault Diagnosis and Early Warning Technology, Anhui Jianzhu University, Hefei 230601, China; luk@ucas.ac.cn
3 School of Engineering Science, University of Chinese Academy of Sciences, Beijing 100049, China
* Correspondence: wangfb@ahjzu.edu.cn; Tel.: +86-551-63828101

Academic Editors: João Manuel R. S. Tavares and Victor Hugo C. de Albuquerque
Received: 2 November 2016; Accepted: 15 February 2017; Published: 22 February 2017

Abstract: Changes in surface topography reflect the state of fatigue damage. In this paper, a new method to characterize metal surface topography during fatigue has been proposed. Firstly, we acquired surface topography images based on machine vision and separated them into roughness, waviness, and form error images through a shearlet transform. Secondly, we constructed gray co-occurrence matrixes of the obtained surface topography images and calculated the characteristic parameters, such as contrast, correlation coefficient, energy, and entropy for all the original and separated images. Then, taking a Q235 steel specimen as an example for testing, the experimental results and theoretical analysis demonstrate that the parameter contrast increases while energy, correlation coefficient and entropy decrease gradually with number of loading circles, which reach their maximum and minimums before fracture, respectively.

Keywords: surface topography; fatigue damage; co-occurrence matrix; shearlet transform

1. Introduction

Surface topography as an important part of machining accuracy not only reflects the surface quality, but also the application performance of components [1]. The evolution of surface topography known as persistent slip bands (PSBs) formation, to which crack nucleation and microcrack propagation are strongly related, could constitute 90% of the fatigue life for some materials. Thus, it is considered as one of the most important tasks to develop a quantitative understanding in studying fatigue.

For metals, fatigue damage is sensitive to surface topography [2]. The surface topography also affects fatigue behavior due to micro- or nano-scale stress levels, stress concentration, and fatigue crack initiation often induced at the bottom of surface profiles [2–4]. In the fatigue damage process accompanying plastic deformation, the internal microstructure of a metal component is distorted. Cyclic hardening or softening changes the microstructure significantly and produces irreversible lattice defects, such as cavity and dislocation. Meanwhile, the surface inclusions and initial holes, slip of the crystal surface, and rotation of grains form surface defects, surface footsteps, and concave convex on the surface, manifesting the changes in surface topography through real-time observation [5–8]. However, it is very difficult to obtain accurate real-time surface topography data, for it evolves slowly and subtly when fatiguing. A scanning electron microscope (SEM) can provide more insight into surface topography and early damage evolution in fatigue, but it cannot provide quantitative information. Using an atomic force microscope (AFM), three-dimensional topographic images of PSBs can be provided, however the imaging area and vertical range of an AFM are limited and it is difficult to operate continual high-speed measurements and apply them to real engineering applications [9].

According to surface filtering theory, the surface topography of a component can be separated into three parts of roughness, waviness, and form error from high to low frequency, whose individual effects can be analyzed [10–12]. As such, surface topography changes during fatigue process can be characterized by using machine vision and texture analysis [13–15].

In this paper, we proposed a method to characterize the relation between material surface micro topography and fatigue properties, through obtaining a high-definition metal surface topography image during fatigue damage and extracting surface texture features by constructing gray co-occurrence matrixes with a fast finite shearlet transform (FFST).

2. Principle of the Shearlet Transform

A shearlet transform is a multiscale signal geometric analysis tool constructed by Guo and Easley et al. through synthesizing expansion affine systems with special forms [16]. By generating a basis function through scale and translation, the shear transformation can produce an optimal sparse representation of multidimensional data with many characteristics, such as multi-resolution analysis, localization, and the directionality and anisotropy of base functions.

2.1. Continuous Shearlet Transform

A two-dimensional continuous shear transform can be written as [17]:

$$SH_{\Phi}f(a,s,t) = \langle f, \phi_{a,s,t} \rangle \tag{1}$$

where $\{\phi_{a,s,t}(x) : s.t.a \in R^{+}, s \in R, t \in R^{2}\}$ is a shearlet base function, which can be represented as:

$$\begin{cases} \phi_{a,s,t}(x) = |\det A_{a,s}|^{-\frac{1}{2}} \phi\left(A_{a,s}^{-1}(x-t)\right) \\ A_{a,s} = A_a B_s = \begin{pmatrix} a & \sqrt{as} \\ 0 & \sqrt{a} \end{pmatrix} = \begin{pmatrix} a & 0 \\ 0 & \sqrt{a} \end{pmatrix} \begin{pmatrix} 1 & s \\ 0 & 1 \end{pmatrix} \end{cases} \tag{2}$$

where A_a is named as parabolic matrix to control the scale and B_s is named shear matrix to control direction, where a, s, t are the parameters of the transform denoted as scale, direction, and displacement respectively.

If $\phi_{a,s,t}(x)$ satisfying admissible conditions can be localized and $f \in L^2(R^2)$ can be expanded with the shearlet base functions, like Equation (3) [18]:

$$\|f\|^2 = \int_{R^2} \int_{-\infty}^{\infty} \int_{0}^{\infty} \langle f, \phi_{a,s,t} \rangle \phi_{a,s,t} \frac{da}{a^3} ds dt \tag{3}$$

When $\vartheta = (\vartheta_1, \vartheta_2) \in R^2, \vartheta_1 \neq 0$ and $\hat{\varphi}(\vartheta_1, \vartheta_2) = \hat{\varphi_1}(\vartheta_1)\hat{\varphi_2}(\vartheta_1/\vartheta_2)$, in which $\hat{\varphi}$ is the Fourier transform of φ, φ_1 and φ_2 are continuous shearlet smooth functions, and the supremums of $\hat{\varphi_2}$, $\hat{\varphi_1}$ satisfy the conditions of $supp\varphi_1 \subset [-2, 1/2] \cup [1/2, 2]$, $supp\varphi_2 \subset [-1, 1]$, then $\varphi_{a,s,t}(x)$ can be represented as Equation (4) in the frequency domain:

$$\begin{cases} \hat{\varphi}_{a,s,t}(\vartheta_1, \vartheta_2) = a^{\frac{3}{4}} e^{-2\pi i \vartheta t} \hat{\varphi_1}(a\vartheta_1) \hat{\varphi_2}\left(a^{-\frac{1}{2}} \frac{\vartheta_2}{\vartheta_1} - s\right) \\ s.t.\vartheta_1 \in \left[-\frac{2}{a}, -\frac{1}{2a}\right] \cup \left[\frac{1}{2a}, \frac{2}{a}\right], \left|\frac{\vartheta_2}{\vartheta_1} - s\right| < \sqrt{a} \end{cases} \tag{4}$$

Thus, the shearlet support composes a pair of trapezoids with different scales in the direction of the relative origin, as shown in Figure 1.

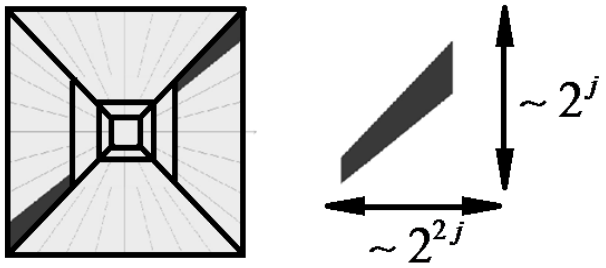

Figure 1. Shearlet frequency domain decomposition (**a**) and support base (**b**).

2.2. Discrete Shearlet Transform

By discretizing the parameters of a, s, t in the space of $L^2(R^2)$, the continuous shearlet transform of $SH_\Phi f(a,s,t)$ constructs a Parseval frame:

$$f(x) = \begin{cases} a_j = 2^{-j}, j = 0, \ldots, J-1 \\ s_{j,k} = k2^{-j}, 2^{-j} \le k \le 2^j \\ t_m = (\frac{m_1}{M}, \frac{m_2}{M}), m = (m_1, m_2) \in Z^2 \end{cases} \tag{5}$$

where $J = \frac{1}{2}\lfloor log_2 N \rfloor$ is a considerable scale. Thus, the continuous shearlet function can be represented in a discretized form:

$$\varphi_{j,k,m}(x) = |detA_{a,s}|^{\frac{1}{2}} \varphi\left(A^{-1}_{a_j, s_{j,k}}(x - t_m)\right) \tag{6}$$

Converting Equation (6) to the frequency domain, it can be rewritten as:

$$\begin{cases} \varphi_{j,k,m}(\vartheta_1, \vartheta_2) = \varphi\left(A^T_{a_j} S^T_{s_{j,k}} \vartheta\right) = \varphi_1(4^{-j}\vartheta_1)\varphi_2\left(2^j \frac{\vartheta_2}{\vartheta_1} + k\right) e^{-2\pi i \langle \vartheta, (\frac{m_1}{M}, \frac{m_2}{M})^T \rangle} \\ s.t. \vartheta_1 = -\left\lfloor \frac{M}{2} \right\rfloor, \ldots, \left\lfloor \frac{M}{2} \right\rfloor - 1,\ \vartheta_2 = -\left\lfloor \frac{N}{2} \right\rfloor, \ldots, \left\lfloor \frac{N}{2} \right\rfloor - 1 \end{cases} \tag{7}$$

In this paper, we used fast finite shearlet transform (FFST) to improve the computational efficiency by fast Fourier transform [19]:

$$SH(f)(l,j,k,m) = \begin{cases} iff2\left(\hat{\varnothing}(\vartheta_1, \vartheta_2),\ \hat{f}(\vartheta_1, \vartheta_2)\right), l = 0 \\ iff2\left(\hat{\varphi}(4^{-j}\vartheta_1, 4^{-j}k\vartheta_1 + 2^{-j}\vartheta_2),\ \hat{f}(\vartheta_1, \vartheta_2)\right), l = h, |k| \le 2^j - 1 \\ iff2\left(\hat{\varphi}(4^{-j}\vartheta_2, 4^{-j}k\vartheta_2 + 2^{-j}\vartheta_1),\ \hat{f}(\vartheta_1, \vartheta_2)\right), l = v, |k| \le 2^j - 1 \\ iff2\left(\hat{\varphi}^{h \times v}(4^{-j}\vartheta_1, 4^{-j}k\vartheta_1 + 2^{-j}\vartheta_2),\ \hat{f}(\vartheta_1, \vartheta_2)\right), l \ne 0, |k| = 2^j \end{cases} \tag{8}$$

where $ff2$ and $iff2$ are the 2D fast Fourier transform (FFT) and the inverse fast Fourier transform (iFFT), respectively, and l is the index of areas corresponding to different frequencies, as shown in Figure 2:

$$\begin{cases} C^h = \left\{(\vartheta_1, \vartheta_2) \in R^2, |\vartheta_1| \ge \frac{1}{2}, |\vartheta_2| < |\vartheta_1|\right\} \\ C^v = \left\{(\vartheta_1, \vartheta_2) \in R^2, |\vartheta_2| \ge \frac{1}{2}, |\vartheta_2| < |\vartheta_1|\right\} \\ C^\times = \left\{(\vartheta_1, \vartheta_2) \in R^2, |\vartheta_1| \ge \frac{1}{2}, |\vartheta_2| \ge \frac{1}{2}, |\vartheta_2| = |\vartheta_1|\right\} \end{cases} \tag{9}$$

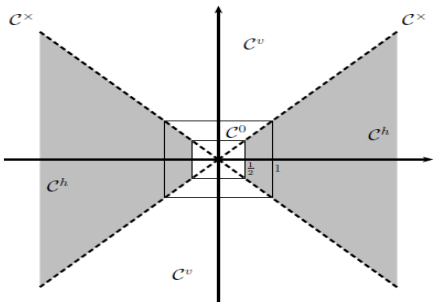

Figure 2. Different areas over which to conduct FFT and iFFT.

Defining $\hat{\varphi}^{h\times v}_{j,k,m} = \hat{\varphi}^{h}_{j,k,m} + \hat{\varphi}^{v}_{j,k,m} + \hat{\varphi}^{\times}_{j,k,m}$, the discretized shearlet transform can be represented as:

$$SH(f)(l,j,k,m,) = \begin{cases} \langle f, \varnothing_m \rangle, |l = 0 \\ \left\langle f, \Phi^{l}_{j,k.m} \right\rangle, |l = \{h,v\} \\ \left\langle f, \Phi^{h\times v}_{j,k.m} \right\rangle, |l = \times, |k| = 2^{j} \end{cases} \tag{10}$$

where $\varnothing_m$ is the scale transform function.

3. Separation of Surface Topography Based on FFST

3.1. Decomposition of Surface Topography

Based on the shearlet transform, to separate the surface topography requires two steps: surface decomposition with the shearlet transform, and reconstruction with an inverse transform based on FFST.

As shown in Figure 3, an N-layer decomposition is done to obtain the shearlet coefficients of various frequencies at different scales through the original image data. Figure 4 shows the basic process for two-layer surface decomposition by FFST.

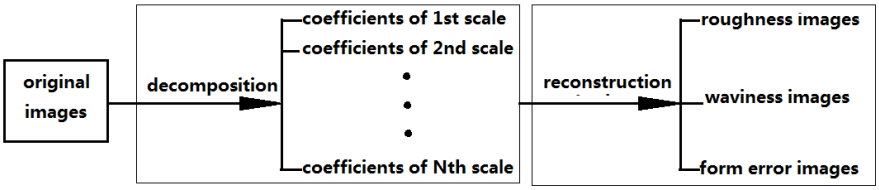

Figure 3. Decomposition and reconstruction of surface topography.

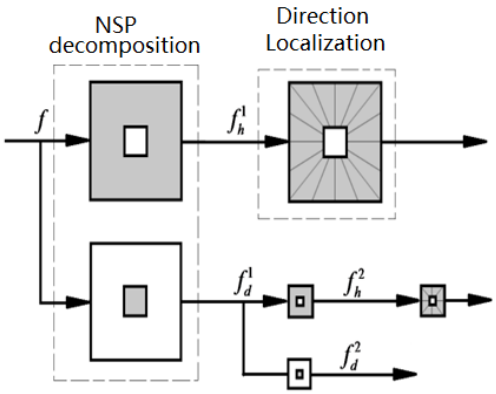

Figure 4. Decomposition operation of surface topography.

In Figure 4, f_h^i and f_l^i, df_h^i, and d_l^i denote the decomposed images and the coefficients with high and low frequencies, respectively. With more decomposed layers, the frequency of the decomposition coefficients increases, thereby including more fine information about the surface texture.

3.2. Reconstruction of Surface Topography

According to surface filtering theory, the surface topography $S(x, y)$, in order from high frequency to low frequency, can be decomposed into roughness $C(x, y)$, waviness $W(x, y)$, and form error $F(x, y)$ with the equation expressed as:

$$S(x, y) = C(x, y) + W(x, y) + F(x, y) \tag{11}$$

Therefore, during the second stage of separating the surface topography, the coefficients obtained by image decomposition in the first stage must be selected on a corresponding scale, on which the images of roughness, waviness, and form error can be reconstructed as follows:

$$\begin{cases} C(x, y) = iFFST\left(df_{h,1}^i, \ldots, df_{h,J}^i, df_{h,1}^K, \ldots, df_{h,J}^K\right) \\ W(x, y) = iFFST\left(df_{h,1}^2, \ldots, df_{h,J}^2, df_{h,1}^K, \ldots, df_{h,N}^K\right) \\ F(x, y) = iFFST\left(df_{l,1}^i\right) \end{cases} \tag{12}$$

3.3. Simulation of Decomposition and Reconstruction for Separating Surface Topography

To validate how separation with a shearlet transform affects surface topography, we simulated a three-dimensional surface with a width of 40 mm and a length of 40 mm, whose surface topography was represented as:

$$S(x, y) = 0.005x + 0.001 \sin(0.4\pi y) + 0.003e(n) \tag{13}$$

In Equation (13), the first term on the right side is the form error, while the second and third terms are the waviness and Gaussian random roughness, respectively. By decomposing the surface topography image simulated with Equation (13) into five scales by FFST, we obtained the decomposition coefficients of the low-frequency and high-frequency bands with 4, 8, 16, 32, and 64 directions.

After that, images of form error, waviness, and roughness were, respectively, reconstructed with the coefficients of the low-frequency and high-frequency bands according to Equation (12). Figure 5 shows the reconstructed images, revealing that the FFST shearlet transform can separate the form error, waviness, and roughness very well.

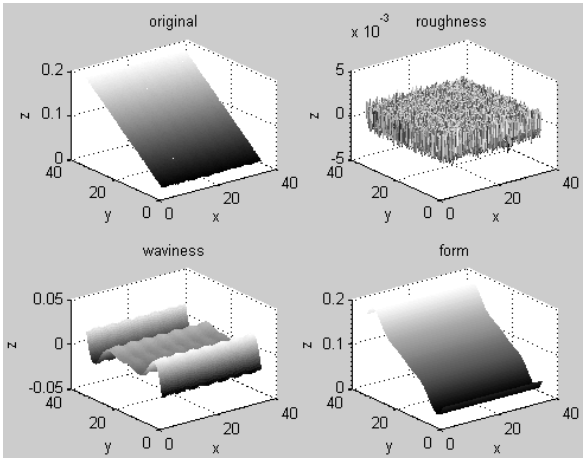

Figure 5. Simulation of separating surface topography.

4. Feature Extraction of Topography Images by a Gray Level Co-Occurrence Matrix

An image of surface topography contains texture characteristics, and the texture that is formed by the gray levels appear repeatedly at the spatial position in the image. Therefore, there exists a certain gray relation among the pixels with a certain distance. The gray level co-occurrence matrix (GLCM), which was proposed by Haralick et al., which reflects the image brightness distribution characteristics, is a common method used to describe the relation mentioned above and can provide more image information about the gray distribution, variation direction, change magnitude, and local region [20].

4.1. Principle of the Gray Level Co-Occurrence Matrix

Suppose the gray level of a pixel $MP(x, y)$ is i, and the gray level of another pixel NP away from MP with distance (Dx, Dy) is j, we define the probability of these two pixels with the gray level (i, j) as:

$$P(i,j,d,\theta) = \left\{ (x,y) \left| \begin{array}{c} f(x,y) = i, \\ f(x+Dx, y+Dy) = j, \\ x = 0, \ldots, M-1, y = 0, \ldots, N-1, \\ i,j = 0, \ldots, L-1 \end{array} \right. \right\} \tag{14}$$

where L is the level number of the image, and θ is the match orientation angle between the pixels, which is often selected as 0°, 45°, 90°, or 135° relative to the reference direction. P is the GLCM, a symmetric matrix whose order number is determined by the number of gray levels in the image.

4.2. Feature Extraction of Image Texture

The GLCM indicates the rule that the two pixel levels appear at a certain match direction within a certain distance and reflects some information of image texture. In the region with coarse texture, the element of the GLCM with greater number in the vicinity of the diagonal for the pixels of coarse texture tend to be the same gray. In the area of fine texture, the elements of the GLCM with a larger number spread to the whole image and away from the diagonal. Until now, researchers have put forward 14 representative parameters to describe GLCM, in which energy, contrast, correlation coefficient and entropy are commonly used in many applications for the fact that they are not correlative [21].

(1) Energy:

$$Energy = \sum_{i=0}^{L-1} \sum_{j=0}^{L-1} p^2(i,j) \tag{15}$$

where $p(i, j, d, \theta)$ is the normalized value of $P(i, j, d, \theta)$. The image energy increases with texture size, and vice versa, which reflects the gray distribution uniformity of the image texture.

(2) Contrast:

$$Contrast = \sum_{n=0}^{L-1} (i-j)^2 \sum_{i=0}^{L-1} \sum_{j=0}^{L-1} p(i,j) \tag{16}$$

The deeper the texture groove, the greater the image contrast, reflecting image clarity.

(3) Correlation coefficient:

$$Correlation = \left(\sum_{i=0}^{L-1} \sum_{j=0}^{L-1} ijp(i,j) - \mu_x \mu_y \right) / \sigma_x^2 \sigma_y^2 \tag{17}$$

where μ_x, μ_y and σ_x, σ_y are the mean and variance of the GLCM elements in the rows and columns. The more obvious the direction texture, the larger the correlation coefficient, which reflects the similarity of texture in a direction.

(4) Entropy:

$$H = \sum_{i=0}^{L-1} \sum_{j=0}^{L-1} p(i,j) \log p(i,j) \tag{18}$$

The more abundant the texture, the greater the entropy, which reflects the information content of the image and can be used to describe minor variations in the image texture.

5. Experiment

5.1. Description

Figure 6 shows the dimensions of the sample used in experiments:

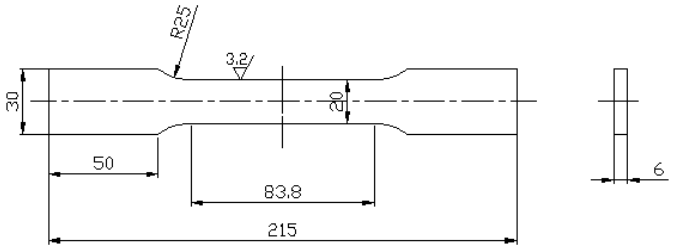

Figure 6. Dimensions of sample (units: mm).

The material of the sample is Q235. The chemical composition was obtained by X-ray fluorescence spectrum analysis (Innov x-5000, INNOV-X, Woburn, MA, USA) and listed in Table 1. The sample was treated by annealing to eliminate residual stress before testing and its yield was about 291.7 MPa, obtained by an electrohydraulic servo fatigue testing machine (SDS-200, Changchun Research Institute for Mechanical Science Co., Ltd., Changchun, China).

Table 1. Chemical composition of the tested Q235 material.

Fe	Mn	Cr	Co	P	S
93.608%	0.147%	0.044%	0.081%	0.042%	0.045%

Before the experiment, both surfaces of the specimen were grinded with sandpaper and cleaned. During the test, the specimen was fixed on an electrohydraulic servo fatigue testing machine, in front of which a high-resolution microscope Celestron 44302 (150×, Celestron, Torrance, CA, USA) was installed, and subjected to a sine load 10 Hz frequency, a maximum amplitude of 192.5 MPa, and mean amplitude of 157.5 MPa.

5.2. Analysis and Discussion

During the experiment operated in a darkroom considering the consistency of illumination, the surface topography of the loaded specimen was imaged every 250 fatigue cycles, and 30 images, including the original image of the unloaded specimen before fracture were obtained, when 7350 fatigue cycles had been loaded.

Accounting for vibration accompanying loading during the fatigue test, a registration procedure has been put into effect on the 30 images to reduce errors before analysis. Each of the images was decomposed into five layers by FFST in turn, and the decomposition coefficients of the low-frequency and high-frequency bands with 4, 8, 16, 32, and 64 directions for various scales were obtained. Similar to the study in Section 2.2, we reconstructed the image of form error, waviness and roughness at different numbers of fatigue cycles with the coefficients of the first scale and low-frequency area, second

and third scales, and fourth and fifth scales, respectively, and the images of the measured surface topography were separated. Figures 7–10 show some results of the decomposition and reconstruction.

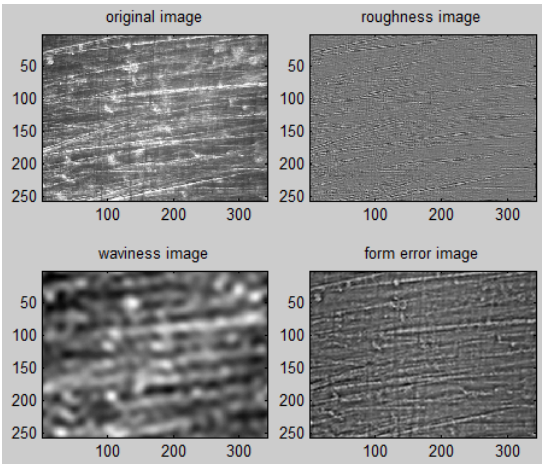

Figure 7. Images of original and decomposed morphologies before testing.

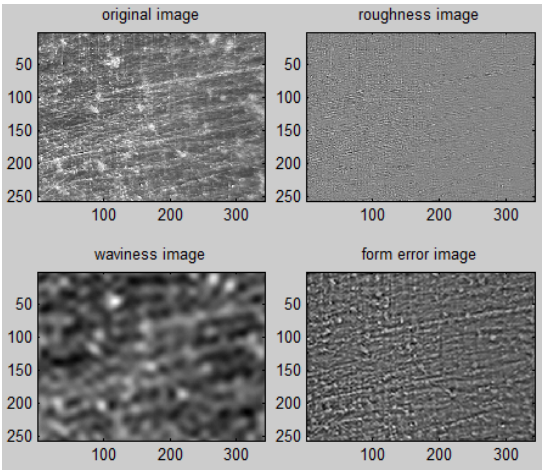

Figure 8. Images of original and decomposed morphologies after loading for 3250 fatigue cycles.

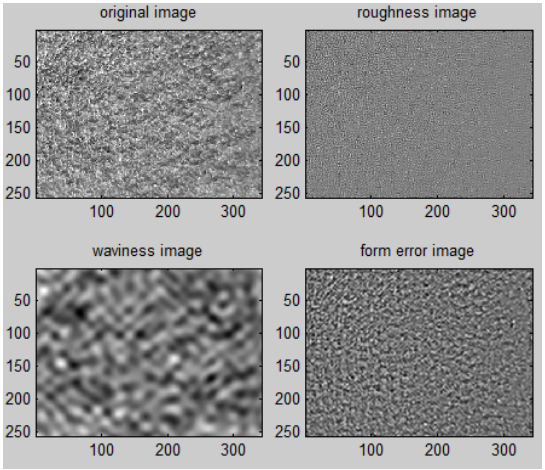

Figure 9. Images of original and decomposed morphologies after loading for 7000 fatigue cycles.

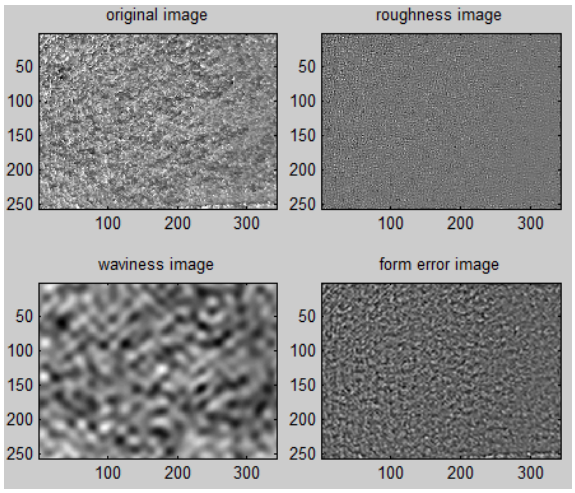

Figure 10. Images of original and decomposed morphologies after loading 7250 fatigue cycles (before fracture).

Figures 7–10 show that with the increase of fatigue loading cycles, the texture of the surface topography image becomes detailed while the existing grooves become deeper, but the correlation coefficients of the image texture along a certain direction decreases. This might be due to the slip band causing the continuous changes of surface texture during the process of fatigue damage.

To further clarify the changes of surface topography during fatiguing, we built and calculated GLCMs for the reconstructed roughness, waviness, form error images, and the corresponding characteristic parameters such as the contrast, correlation coefficient, energy, and entropy, as shown in Figures 11–14.

It can be seen from Figures 11–14 that:

(1) As fatigue load is applied, the contrast of the surface topography image increases to a maximum, and then decreases before fracture. This occurs mainly because the stress concentration initiates microcracks on the surface and deepens pre-existing crack grooves. As fatigue loading continues, the specimen gradually draws closer to failure, the internal elastic energy releases, and the contrast of the surface topography image decreases.

(2) With fatigue loading, the image correlation coefficient, energy, and entropy decrease and reach their minimums before fracture. The reason perhaps is that the surface grooves deform and the surface texture becomes finer due to "intrusion-extrusion" effects, weakening the texture similarity in all directions and changing it from striped to non-striped.

(3) The decomposition images of roughness obtained by FFST are more similar to the raw images of texture than to the images of waviness and form error. The reason might be that the experimental images are taken of a surface topography in which the surface roughness is more prominent and the fatigue damage manifested firstly as changes in roughness. Moreover, the images of waviness and form error can provide more data useful in recognizing fatigue damage, revealing certain heuristics.

(4) The features of 0° change are more remarkable than those in the other directions. This behavior illustrates that the changes in surface topography with fatigue damage are related to not only the gripping points at the two ends of the specimen, the modes of telescope vertical fixation, and the push-pull impact fatigue testing, but also the direction of fatigue damage.

In order to illustrate the performance of the method proposed in the work, we compare the results with those obtained from a conventional approach using TRscan301 white light confocal microscope made by Swiss Trimos TR Scan (TRIMOS, Renens, Switzerland). Since online real-time monitoring cannot be carried out with this instrument, we selected 10 groups of samples with good consistency

and conducted the fatigue experiments with the samples one by one. Then the samples with the different fatigue damage extent were obtained. By scanning the same areas of the testing samples, a flurry of surface topography data, being defined in ISO 25178, were acquired. It was found that the three-dimensional surface parameters (including amplitude, space, function, and comprehensive parameters) were changed with the increase of the fatigue damage degree, but the change rules of the parameters were not clear, due to the complexity. These change rules will be explored in further study late. In addition, both the 3D surface topography information of white light confocal images and that of the gray image features obtained by the method proposed in this paper, are related to the extent of fatigue damage, but the essence of these two concepts is different. The results of preliminary comparison experiments showed that the gray level image processing method has a high efficiency and is convenient for real engineering applications, for the topography parameters are easy to be extracted and the corresponding consuming time is only 1/60–1/100 of that for the white light confocal method, which is not suitable for online detection for many parameters and a very large amount of data must be processed.

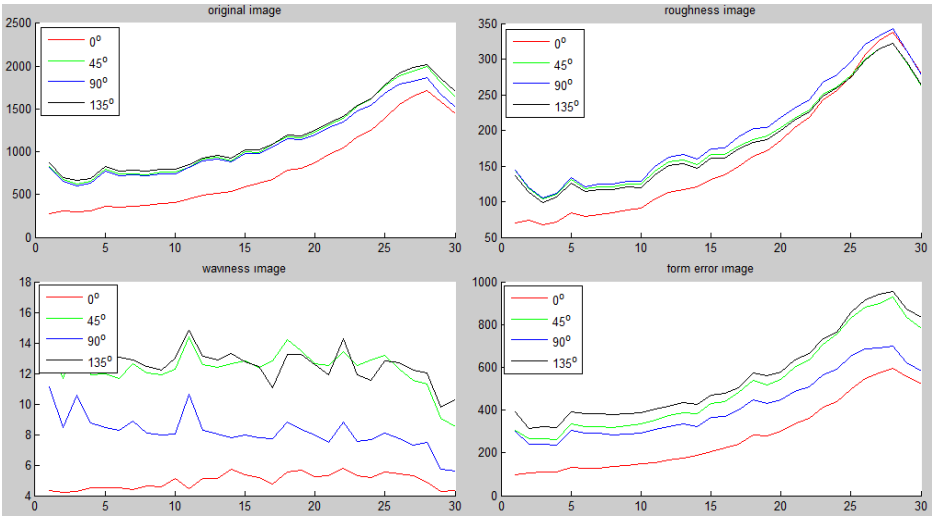

Figure 11. Contrast.

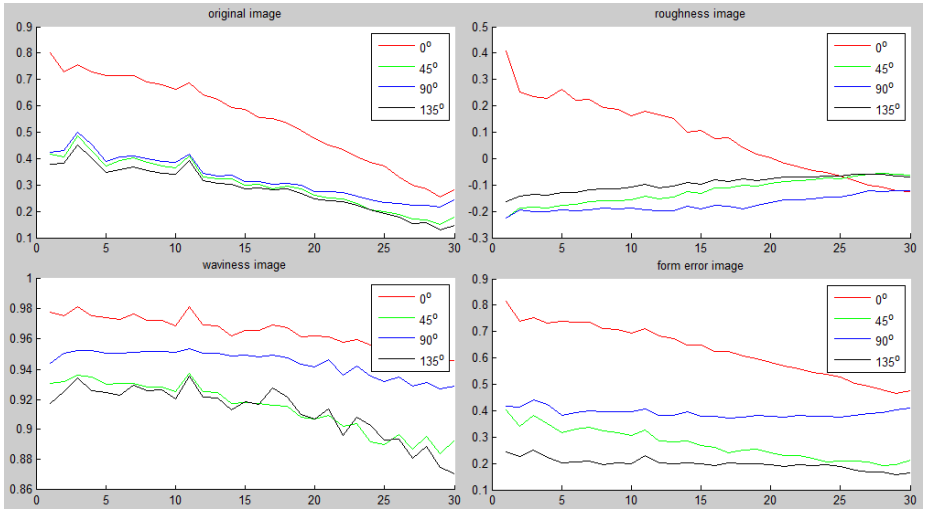

Figure 12. Correlation coefficient.

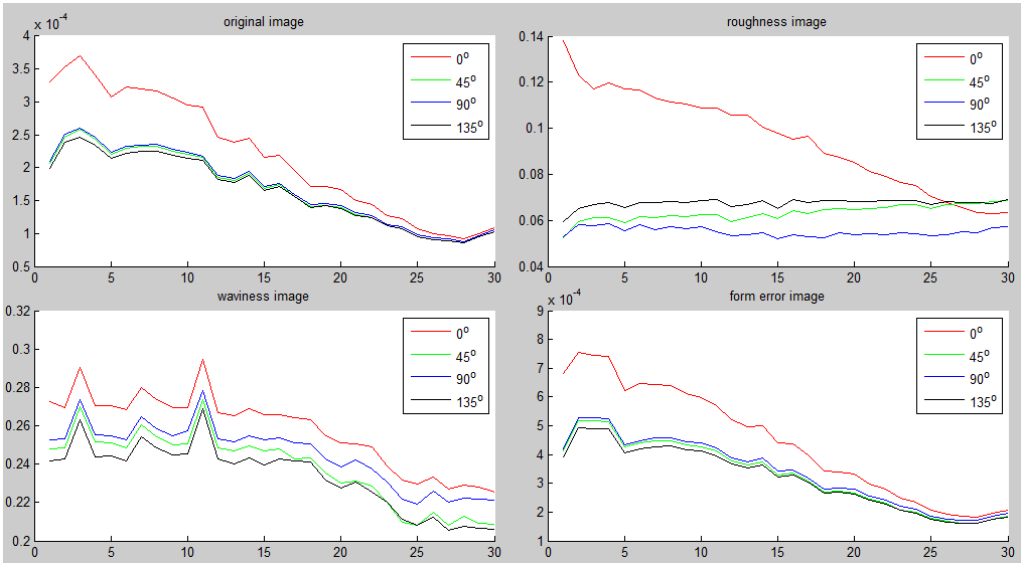

Figure 13. Energy.

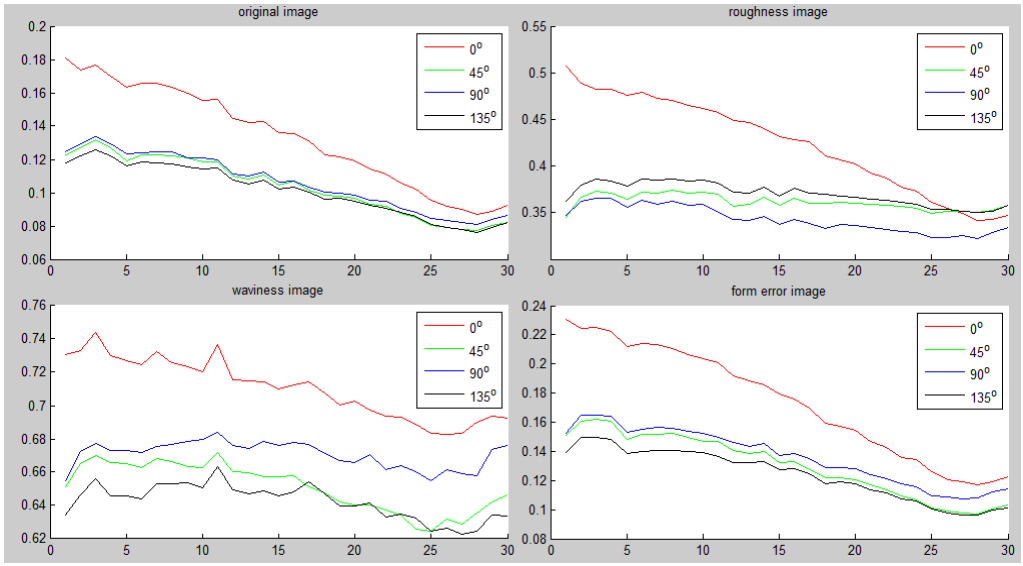

Figure 14. Entropy.

6. Conclusions

The state of fatigue damage can be reflected by the changes in surface topography. In order to characterize the metal surface topography during fatiguing processes, a new method was proposed. In this method, the machine vision was used to obtain the surface topography, which was then separated by FFST. After that, the images of roughness, waviness, and form error were reconstructed. The gray level co-occurrence matrices and the corresponding characteristic parameters of the above images and the original ones were built and calculated.

The results obtained from this investigation showed that the increase of the loading cycle number caused the finer texture of the metal surface, as well as deeper grooves. For the surface topography, the image contrast increased to its maximum and the energy, correlation coefficient, and entropy decreased to their minimum values before fracture failure.

This investigation will provide an early warning way to the real-time state for the fatigue damage of metal components. In the future, further investigations will be conducted to find the relationships

among the above results through the method of surface image processes with fatigue mechanisms and fatigue damage.

Acknowledgments: This work was supported by the National Natural Science Foundation of China (No. 61372094), the Natural Science Foundation of Anhui Province (No. 1508085QE91), the Natural Science Research Project of Education Department of Anhui Province (No. KJ2015JD23), and the Anhui Jianzhu University PhD Start-up Foundation (No. 2015QD04).

Author Contributions: Darong Zhu conceived the idea and designed the experiments. Lu Xu, Fangbin Wang and Tao Liu performed the experiments, analyzed the data and wrote the paper. Ke Lu contributed with advice on the method of analysis.

Conflicts of Interest: The authors declare no conflict of interest.

References

1. Whitehouse, D.J. Surface metrology. *Meas. Sci. Technol.* **1997**, *8*, 955–972. [CrossRef]
2. Ardi, D.T.; Li, Y.G.; Chan, K.H.K.; Blunt, L.; Bache, M.R. The effects of machined topography on fatigue life of a nickel based super alloy. *Procedia CIRP* **2014**, *13*, 19–24. [CrossRef]
3. Gao, Y.X.; Yi, J.Z.; Lee, P.D.; Lindley, T.C. A micro-cell model of the effect of microstructure and defects on fatigue resistance in cast aluminum alloys. *Acta Mater.* **2004**, *52*, 5435–5449. [CrossRef]
4. Meng, B.; Guo, W.L.; Jiang, Y. Effect of surface topography on micro-mechanical behavior for different metallic materials. *J. Aeronaut. Mater.* **2006**, *26*, 18–23. (In Chinese)
5. Sachtleber, M.; Raabe, D.; Weiland, H. Surface roughening and color changes of coated aluminum sheets during plastic straining. *J. Mater. Process. Technol.* **2004**, *148*, 68–76. [CrossRef]
6. Wichern, C.M.; Cooman, B.C.D.; Tyne, C.J.V. Surface roughness changes on a hot-dipped galvanized sheet steel during deformation at low strain levels. *Acta Mater.* **2004**, *52*, 1211–1222. [CrossRef]
7. Shigemi, S.; Yasuo, O. Some experimental studies of fatigue slip bands and persistent slip bands during fatigue process of low-carbon steel. *Eng. Fract. Mech.* **1979**, *12*, 531–540. [CrossRef]
8. Ummenhofer, T.; Medgenberg, J. Numerical modelling of thermoelasticity and plasticity in fatigue-loaded low carbon steel. *Quant. Infrared Thermogr. J.* **2006**, *3*, 71–91. [CrossRef]
9. Wang, Y.; Meletis, E.I.; Huang, H. Quantitative study of surface roughness evolution during low-cycle fatigue of 316L stainless steel using Scanning Whitelight Interferometric (SWLI) Microscopy. *Int. J. Fatigue* **2013**, *48*, 280–288. [CrossRef]
10. Liu, C.; Du, S.; Xi, L. Shearlet-based filtering method for three-dimensional engineering surfaces. *Mach. Des. Res.* **2014**, *40*, 70–76. (In Chinese)
11. Wang, M.; Xi, L.; Du, S. 3D surface form error evaluation using high definition metrology. *Precis. Eng.* **2014**, *38*, 230–236. [CrossRef]
12. Suriano, S.; Wang, H.; Hu, S.J. Sequential monitoring of surface spatial variation in automotive machining processes based on high definition metrology. *J. Manuf. Syst.* **2012**, *31*, 8–14. [CrossRef]
13. Yang, G.G. *Modern Optical Testing Technology*; Zhejiang University Press: Hangzhou, China, 2004.
14. Tong, X.Y.; Li, H.X.; Yao, L.J.; Li, B. Feature extraction and analysis of surface microscopic image of pure copper subjecting low cycle fatigue. *Mech. Sci. Technol. Aerosp. Eng.* **2015**, *34*, 1446–1450. (In Chinese)
15. Liu, L.; Kuang, G.Y. Overview of image textural feature extraction method. *J. Image Graph.* **2009**, *14*, 622–635. (In Chinese)
16. Guo, K.; Labate, D. Optimally sparse multidimensional representation using shearlets. *SIAM J. Math Anal.* **2007**, *39*, 298–318. [CrossRef]
17. Li, B.; Tang, C.; Zhu, X.; Su, Y.; Xu, W. Shearlet transform for phase extraction in fringe projection profilometry with edges discontinuity. *Opt. Lasers Eng.* **2016**, *78*, 91–98. [CrossRef]
18. Labate, D.; Lim, W.Q.; Kutyniok, G.; Weiss, G. Sparse Multidimensional Representation using Shearlets. *SPIE. Digit. Libr.* **2005**. [CrossRef]
19. Häuser, S.; Steidl, G. Convex multiclass segmentation with shearlet regularization. *Int. J. Comput. Math.* **2013**, *90*, 62–81. [CrossRef]

20. Haralick, R.M.; Shanmugam, K.; Dinstei, I.H. Textural feature for image classification. *IEEE Trans. Syst. Man Cybern.* **1975**, *SMC-3*, 610–621. [CrossRef]
21. Wang, Z.Z. *Research on the Classification Method of Remote Sensing Images Based on Texture and Spectral Information Fusion*; Xi'an Electronic and Science University: Xi'an, China, 2010. (In Chinese)